A meshless fragile points method for the solution of the monodomain model for cardiac electrophysiology simulation

Konstantinos A. Mountris [a,b,*], Leiting Dong [c], Yue Guan [d], Satya N. Atluri [d], Esther Pueyo [a,b]

[a] *Aragón Institute for Engineering Research, University of Zaragoza, IIS Aragón, Zaragoza, Spain*
[b] *CIBER in Bioengineering, Biomaterials & Nanomedicine (CIBER-BBN), Spain*
[c] *Beihang University, Beijing, China*
[d] *Texas Tech University, Lubbock, TX, United States of America*

ARTICLE INFO

ABSTRACT

Meshless methods for in silico modeling and simulation of cardiac electrophysiology are gaining more and more popularity. These methods do not require a mesh and are more suitable than the Finite Element Method (FEM) to simulate the activity of complex geometrical structures like the human heart. However, challenges such as numerical integration accuracy and time efficiency remain, which limit their applicability. Recently, the Fragile Points Method (FPM) has been introduced in the meshless methods family. It uses local, simple, polynomial, discontinuous functions to construct trial and test functions in the Galerkin weak form. This allows for accurate integration and improved efficiency while enabling the imposition of essential and natural boundary conditions as in FEM. In this work, we consider the application of FPM for cardiac electrophysiology simulation. We derive the cardiac monodomain model using the FPM formulation and we solve several benchmark problems in 2D and 3D. We show that FPM leads to solutions of accuracy and efficiency similar to FEM while alleviating the need for a mesh. Additionally, FPM demonstrates comparable convergence to FEM in the considered benchmarks.

1. Introduction

The Finite Element Method (FEM) is widely used for simulating cardiac electrophysiology mainly due to its robustness and accuracy [1]. However, accuracy is substantially deteriorated when the mesh undergoes a large deformation or if it does not satisfy specific quality criteria [2]. For this reason, in recent years there has been growing interest in alternative meshless methods that partially or completely alleviate the mesh-related limitations of FEM. Several meshless methods have been investigated so far in the context of cardiac electrophysiology.

The element-free Galerkin (EFG) method offers high convergence rate [3] and it has been used successfully in several applications [4,5]. It has been used in cardiac electrophysiology to solve the cardiac monodomain equation using a meshless representation of the Auckland heart model [6]. EFG employs the Moving Least Squares (MLS) approximation [7] for the solution of the Galerkin weak form. Therefore, the imposition of essential boundary conditions requires special treatment due to the lack of the Kronecker delta property in MLS. To solve this issue, Maximum Entropy (MaxEnt) approximants [8,9] have been proposed as an alternative to MLS in EFG [10]. Due to the weak Kronecker delta property of MaxEnt, the influence of internal nodes on the boundary of the domain of interest is eliminated and essential boundary conditions can be imposed directly as in FEM. However, the MaxEnt approximation functions are significantly more complex than MLS. As a result, a large number of quadrature points is required to deal with the quadrature accuracy problem of meshless methods [11,12].

On the other hand, the Mixed Collocation Method (MCM) [13,14] is a purely meshless method that avoids the quadrature accuracy problem. It has been used for the simulation of the cardiac monodomain model demonstrating results in good agreement with FEM [15,16]. MCM is a variation of the Meshless Local Petrov–Galerkin method [17] where the Dirac delta distribution is used as test function and interpolation is applied both on the field function and its gradient [17–19]. As a result, the integrals in the Petrov–Galerkin weak form are replaced with nodal summation. In addition, essential boundary conditions are imposed directly through collocation. However, being a collocation method, it usually requires the construction of support domains with a large number of collocation points to avoid inaccuracy during the imposition of natural boundary conditions [20] and may not be as efficient as FEM in large-scale 3D problems.

Table 1

Characteristics of FPM and other numerical methods as in [24].

Method	Trial function	Weak/strong form	Numerical integration
FEM	element-based	Galerkin weak form	Gauss integration, inaccurate for highly distorted elements
EFG	point-based continuous	Galerkin weak form	numerical integration with many points
MLPG	point-based continuous	local Petrov–Galerkin weak form	numerical integration with many points in local support domain
FPM	point-based discontinuous	Galerkin weak form with numerical flux corrections	exact integration with one-point-integral for linear trial functions

Very recently, a novel meshless technique going by the name of Fragile Points Method (FPM) has been added to the artillery of meshless methods [21]. FPM uses local, simple, polynomial, discontinuous functions [22] as trial and test functions for the solution of the Galerkin weak form. Using these polynomial trial and test functions, the integration in the Galerkin weak form becomes trivial. Due to the simplicity of the test and trial functions, single-point integration is sufficient to compute integrals with high accuracy in FPM. We refer to Table 1 for a comparison of integration in FPM and other meshless methods. Moreover, both essential and natural boundary conditions can be imposed as in FEM. However, due to the discontinuity of the trial and test functions, the assembly of the FPM point stiffness matrices leads to an inconsistent global stiffness matrix. To remedy this issue, the numerical flux corrections, which are widely used in Discontinuous Galerkin methods [23], are employed in FPM to obtain a consistent, sparse and symmetric global stiffness matrix.

Despite being only recently introduced, FPM has been demonstrated to be an accurate and efficient method with many desired properties (i.e. accurate integration, exact imposition of boundary conditions) and has been already employed to solve linear elasticity [24], heat conduction [25,26] and flexoelectric problems with crack propagation [27]. In the following, we use the abbreviation FPM to exclusively refer to the Fragile Points Method, which should not be confused with other methods previously introduced in the literature that used the FPM abbreviation, like the Finite Point Method [28], Finite Pointset Method [29] and Finite Particle Method [30].

In the present study, we employ FPM for the solution of the cardiac monodomain model. Our motivation is to provide a meshless alternative to FEM for cardiac electrophysiology simulation, while maintaining accuracy and efficiency. The paper is structured as follows. In Section 2, we describe the theoretical aspects of FPM and the derivation of the cardiac monodomain models. In Section 3, we present several numerical examples where FPM is applied to simulate electrophysiology in both 2D and 3D benchmark problems, as well as in a large scale biventricular geometry under myocardial infarction conditions. Finally, in Section 4, we provide our concluding remarks.

2. Cardiac monodomain model FPM formulation

2.1. The cardiac monodomain equation

We consider the cardiac monodomain model for the simulation of electrical impulse propagation in the human heart, which is governed by the following reaction–diffusion partial differential equation (PDE) [31]:

$$\partial V(t)/\partial t = -(I_{ion}(V(t)) + I_{stim}(t))/C + \nabla \cdot (D\nabla V(t)) \quad \text{in } \Omega$$
$$n \cdot (D\nabla V(t)) = 0 \quad \text{in } \partial\Omega \tag{1}$$

where $\partial V/\partial t$ denotes the transmembrane voltage time derivative, $I_{ion}(V(t))$ the total ionic current, $I_{stim}(t)$ the external stimulus current, C the cell capacitance per unit surface area and D the diffusion tensor.

Ω and $\partial\Omega$ are the domain of interest and its boundary and n is the outward unit vector normal to the boundary.

The diffusion tensor D is given by:

$$D = d_0 \left[(1 - \rho) f \otimes f + \rho I \right] \tag{2}$$

where d_0 denotes the diffusion coefficient along the cardiac fiber direction, f the cardiac fiber direction vector, $\rho \leq 1$ the transverse-to-longitudinal conductivity ratio, I the identity matrix and $\otimes$ the tensor product operator.

We employ the operator splitting technique to obtain the decoupled system of Eq. (1):

$$\partial V(t)/\partial t = -(I_{ion}(V(t)) + I_{stim}(t))/C \quad \text{in } \Omega$$
$$\partial V(t)/\partial t = \nabla \cdot (D\nabla V(t)) \quad \text{in } \Omega \tag{3}$$
$$n \cdot (D\nabla V(t)) = 0 \quad \text{on } \partial\Omega$$

The decoupled system can be solved efficiently by applying either the Godunov (first-order) or Strang (second-order) methods [32]. In the following, we consider the total ionic current I_{ion} of Eq. (3) normalized by the capacitance C.

2.2. Computation of trial and test functions in FPM

FPM is a meshless method where trial and test functions are established on arbitrarily distributed points in the domain of interest Ω. Unlike mesh-based methods, such as FEM, connectivity information is not required. Simple, local, polynomial trial functions are defined in compact support domains, formed by partitioning the domain in conforming and nonoverlapping subdomains around each point. The partition is not unique and can include subdomains of arbitrary shape, such as polygons that can be obtained by the Voronoi diagram partition.

We define the trial functions at each subdomain in terms of the transmembrane voltage V and its gradient ∇V. The trial function V_h for subdomain E_0 that contains the point P_0 is given by:

$$V_h(x) = V_0 + (x - x_0) \cdot \nabla V \big|_{P_0}, \tag{4}$$

where x is the coordinate vector of a point in E_0, V_0 is the value of V_h at P_0, x_0 is the coordinate vector of P_0 and $\nabla V \big|_{P_0}$ (i.e. the voltage gradient at P_0) is unknown. To compute $\nabla V \big|_{P_0}$, we employ the Generalized Finite Difference (GFD) method [22] to minimize the weighted discrete L^2 norm:

$$J = \sum_{i=1}^{m} w_i \left[(x_i - x_0) \cdot \nabla V \big|_{P_0} - (V_i - V_0) \right]^2, \tag{5}$$

where x_i denotes the coordinate vector of $P_i \in E_0$, V_i denotes the value of V_h at P_i and w_i denotes the value of the weight function at P_i ($i = 1, 2, \ldots, m$), with m being the number of points in the support domain of P_0. We should note that a compact support domain for P_0 is defined by the points in the first ring of adjacent subdomains to the subdomain of P_0 (Fig. 1). Assuming constant weight functions, we obtain the transmembrane voltage gradient at P_0 by:

$$\nabla V \big|_{P_0} = B V_E, \tag{6}$$

where

$$V_E = \begin{bmatrix} V_0 & V_1 & V_2 & \ldots & V_m \end{bmatrix}^T,$$
$$B = (A^T A)^{-1} A^T \begin{bmatrix} I_1 & I_2 \end{bmatrix},$$
$$I_1 = \begin{bmatrix} -1 \\ -1 \\ \vdots \\ -1 \end{bmatrix}_{m \times 1}, \quad I_2 = \begin{bmatrix} 1 & 0 & \ldots & 0 \\ 0 & 1 & \ddots & \vdots \\ \vdots & \ddots & \ddots & 0 \\ 0 & \ldots & 0 & 1 \end{bmatrix}_{m \times m}, \quad A = \begin{bmatrix} x_1 - x_0 \\ x_2 - x_0 \\ \vdots \\ x_m - x_0 \end{bmatrix}. \tag{7}$$

Using Eq. (6), the trial function $V_h(x)$ can be obtained by:

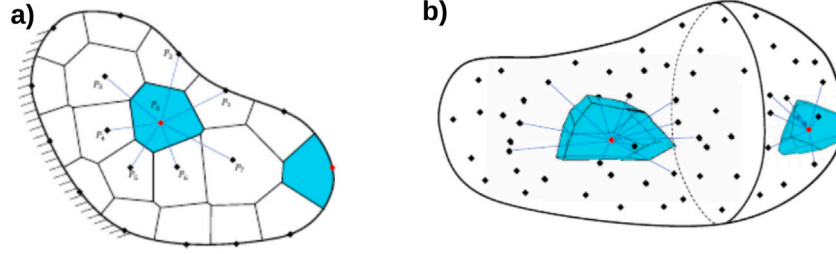$$V_h(x) = N V_E, \quad x \in E_0 \tag{8}$$

Fig. 1. (a) Partition of 2D domain with randomly distributed points inside and on its boundary (points $P \in \Omega \cup \partial\Omega$). (b) Partition of 3D domain with randomly distributed points inside it (points $P \in \Omega$).

where N denotes the shape function of V_h in E_0:

$$N = [\boldsymbol{x} - \boldsymbol{x}_0]\boldsymbol{B} + \begin{bmatrix} 1 & 0 & \dots & 0 \end{bmatrix}_{1\times(m+1)}. \tag{9}$$

Since the shape function is defined in each subdomain independently, it can be discontinuous at the internal boundaries. The Galerkin weak form in FPM is established by constructing both the trial and test functions using Eq. (8). It should be noted that due to the discontinuity of the trial and test functions, the Galerkin weak form will lead to an inconsistent matrix and inaccurate results. Therefore, numerical flux corrections, which are common in Discontinuous Galerkin Finite Element Method [23], are introduced in FPM to remedy this issue.

2.3. Numerical flux corrections to remedy the inconsistency

We address the inconsistency issue by employing the Interior Penalty (IP) numerical flux corrections [33]. We start by writing the Galerkin weak form of Eq. (3) for each subdomain $E \in \Omega$, which is given by:

$$\int_E v\frac{\partial V_h}{\partial t}d\Omega + \int_E \nabla v^T \boldsymbol{D}\nabla V_h d\Omega = \int_{\partial E} v\boldsymbol{n}^T\boldsymbol{D}\nabla V_h d\Gamma, \tag{10}$$

where v and V_h are the test and trial functions, respectively, ∂E is the boundary of the subdomain E, $\boldsymbol{n}$ denotes the outward normal vector to ∂E, and Γ denotes the set of internal and external boundaries, i.e., $\Gamma = \Gamma_h + \partial\Omega = \Gamma_h + \Gamma_N$, where Γ_h is the set of internal boundaries.

Next, the jump operator $[\![\ ]\!]$ and average operator $\{\ \}$ are used to sum Eq. (10) over all subdomains [26]:

$$\sum_{E\in\Omega}\int_E v\frac{\partial V_h}{\partial t}d\Omega + \int_E \nabla v^T \boldsymbol{D}\nabla V_h d\Omega = \sum_{e\in\Gamma_N}\int_e [\![v]\!]\{\boldsymbol{n}^T\boldsymbol{D}\nabla V_h\}d\Gamma +$$
$$\sum_{e\in\Gamma_h}\int_e \{v\}[\![\boldsymbol{n}^T\boldsymbol{D}\nabla V_h]\!]d\Gamma + \sum_{e\in\Gamma_h}\int_e [\![v]\!]\{\boldsymbol{n}^T\boldsymbol{D}\nabla V_h\}d\Gamma, \tag{11}$$

where the jump operator $[\ ]$ and average operator $\{\ \}$ are given, $\forall w \in \mathbb{R}$, by:

$$[\![w]\!] = \begin{cases} w|_e^{E1} - w|_e^{E2} & e \in \Gamma_h \\ w|_e & e \in \partial\Omega, \end{cases} \quad \{w\} = \begin{cases} \frac{1}{2}\left(w|_e^{E1} + w|_e^{E2}\right) & e \in \Gamma_h \\ w|_e & e \in \partial\Omega. \end{cases} \tag{12}$$

When $e \in \Gamma_h$ $(e \in \partial E_1 \cap \partial E_2)$, $\boldsymbol{n}$ is a unit vector normal to $e \in \Gamma_h$ and pointing outward from E.

Substituting the boundary conditions (Eq. (3)) into Eq. (11), we obtain:

$$\sum_{e\in\Gamma_N}\int_e [\![v]\!]\{\boldsymbol{n}^T\boldsymbol{D}\nabla V_h\}d\Gamma = 0. \tag{13}$$

Additionally, $[\![\boldsymbol{n}^T\boldsymbol{D}\nabla V_h]\!] = 0$ and $[\![V_h]\!] = 0$ when V_h is the exact solution since there is no jump in the internal boundaries. As a result, $\{\boldsymbol{n}^T\boldsymbol{D}\nabla v\}[\![V_h]\!] = 0$ and we can replace the term $\{v\}[\![\boldsymbol{n}^T\boldsymbol{D}\nabla V_h]\!]$ in Eq. (11) with $\{\boldsymbol{n}^T\boldsymbol{D}\nabla v\}[\![V_h]\!]$ without affecting the accuracy of the formula.

Finally, the internal penalty numerical flux is applied on Γ_h with penalty parameter η to obtain the consistent FPM formula [25]:

$$\sum_{E\in\Omega}\int_E v\frac{\partial V_h}{\partial t}d\Omega + \int_E \nabla v^T\boldsymbol{D}\nabla V_h d\Omega - \sum_{e\in\Gamma_h}\int_e \{\boldsymbol{n}^T\boldsymbol{D}\nabla V_h\}[\![v]\!]d\Gamma -$$
$$\sum_{e\in\Gamma_h}\int_e \{\boldsymbol{n}^T\boldsymbol{D}\nabla v\}[\![V_h]\!]d\Gamma + \sum_{e\in\Gamma_h}\frac{\eta}{h_e}\int_e [\![V_h]\!][\![v]\!]d\Gamma = 0, \tag{14}$$

where h_e is a boundary-dependent parameter with the unit of length. In this work, we define h_e as the distance between points i, j when $e \in \partial E_i \cap \partial E_j$. The penalty parameter η, $\eta > 0$, has the same units as $\boldsymbol{D}$ and is independent of the boundary size. It should be noted that the penalty parameter should be large enough to ensure stability, but excessively large values should be avoided since they may cause a condition number problem. An extensive discussion on recommended values for the penalty parameter can be found in [25]. In this work, we use η given by:

$$\eta = p * \frac{\sum_i^m \mathcal{V}_{E_i}\bar{d}_i}{\sum_i^m \mathcal{V}_{E_i}}, \tag{15}$$

where p is a penalty coefficient, $\mathcal{V}_{E_i}$ denotes the volume of the cell containing the ith of the m points in the support domain, and $\bar{d}_i$ is the mean value of the diagonal entries in the diffusion tensor $\boldsymbol{D}_i$ of the ith point.

2.4. Numerical implementation

The formula of FPM can be written in matrix form:

$$C\dot{V} + KV = 0, \tag{16}$$

where C and K denote the global normalized capacity and diffusion matrices, respectively, and V is the unknown vector collecting the nodal values of the transmembrane potential.

To assemble the global matrices C and K, we substitute the shape function N for V_h and v and matrix B for ∇V_h and ∇v in Eq. (14) to obtain the point normalized capacity matrix C_E, the point diffusion matrix K_E, and the internal boundary diffusion matrix K_h:

$$C_E = \int_E \boldsymbol{N}^T\boldsymbol{N}d\Omega, \quad E \in \Omega,$$

$$K_E = \int_E \boldsymbol{B}^T\boldsymbol{D}\boldsymbol{B}d\Omega, \quad E \in \Omega,$$

$$K_h = -\frac{1}{2}\int_e (\boldsymbol{N}_1^T\boldsymbol{n}_1^T\boldsymbol{D}_1\boldsymbol{B}_1 + \boldsymbol{B}_1^T\boldsymbol{D}_1^T\boldsymbol{n}_1\boldsymbol{N}_1)d\Gamma + \frac{\eta}{h_e}\int_e \boldsymbol{N}_1^T\boldsymbol{N}_1 d\Gamma$$
$$-\frac{1}{2}\int_e (\boldsymbol{N}_2^T\boldsymbol{n}_2^T\boldsymbol{D}_2\boldsymbol{B}_2 + \boldsymbol{B}_2^T\boldsymbol{D}_2^T\boldsymbol{n}_2\boldsymbol{N}_2)d\Gamma + \frac{\eta}{h_e}\int_e \boldsymbol{N}_2^T\boldsymbol{N}_2 d\Gamma$$
$$-\frac{1}{2}\int_e (\boldsymbol{N}_1^T\boldsymbol{n}_1^T\boldsymbol{D}_2\boldsymbol{B}_2 + \boldsymbol{B}_1^T\boldsymbol{D}_1^T\boldsymbol{n}_2\boldsymbol{N}_2)d\Gamma - \frac{\eta}{h_e}\int_e \boldsymbol{N}_1^T\boldsymbol{N}_2 d\Gamma$$
$$-\frac{1}{2}\int_e (\boldsymbol{N}_2^T\boldsymbol{n}_2^T\boldsymbol{D}_1\boldsymbol{B}_1 + \boldsymbol{B}_2^T\boldsymbol{D}_2^T\boldsymbol{n}_1\boldsymbol{N}_1)d\Gamma - \frac{\eta}{h_e}\int_e \boldsymbol{N}_2^T\boldsymbol{N}_1 d\Gamma, \tag{17}$$
$$e \in \partial E_1 \cap \partial E_2.$$

The assembly of global matrices C and K is performed as in FEM, where C is obtained by assembling all the individual capacity point matrices C_E, and K is obtained by assembling all the point diffusion K_E

Table 2

Required execution time for FPM and FEM solutions for the numerical examples in Section 3.

Electrical propagation in a 2D ventricular tissue (Section 3.1)					
ℓ (mm)	t_{FEM} (min)	t_{FPM} (min)			
		$p = 1$	$p = 2$	$p = 5$	$p = 10$
2	0.87	0.90	0.95	0.88	0.84
1	1.52	1.59	1.63	1.51	1.51
0.5	3.7	3.65	3.77	3.76	4.21
0.25	12.33	12.46	12.47	14.98	17.26

Acetylcholine-induced effects in human atrial electrical activity (Section 3.2)		
ACh (μM)	t_{FEM} (min)	t_{FPM} (min)
0.00	13.04	15.21
0.02	13.82	15.49
0.04	13.26	15.42
0.06	13.62	14.67
0.08	14.62	15.93
0.10	13.26	14.61

Electrical propagation in a benchmark 3D cuboid geometry (Section 3.3)		
ℓ (mm)	t_{FEM} (min)	t_{FPM} (min)
0.5	0.35	0.38
0.2	2.94	3.26
0.1	27.9	29.25

Simulation of electrical activation in 3D biventricular infarction model (Section 3.4)		
pacing	t_{FEM} (min)	t_{FPM} (min)
basal	9.37	11.52
apical	9.15	11.46

and internal boundary diffusion matrices K_h. It should be noted that the resulting global diffusion matrix is symmetric, sparse, and positive definite. Finally, Eq. (16) can be solved with a time discretization based on a θ-rule. Assuming that the current solution $V^n = V(t_n)$ is known, we can compute the solution at the next time step V^{n+1} from the θ-rule as given below:

$$C\frac{V^{n+1} - V^n}{dt} + \theta K V^{n+1} + (1 - \theta)K V^n = 0, \tag{18}$$

where $\frac{V^{n+1} - V^n}{dt}$ is the forward finite difference form of $\dot{V}$, dt is the time step, and $\theta \in [0, 1]$. Eq. (18) is written in the form $Ax = b$ to obtain:

$$(C + dt\theta K)V^{n+1} = [C - dt(1 - \theta)K]V^n. \tag{19}$$

In what follows, we solve Eq. (19) using the standard Forward Euler scheme ($\theta = 0$). We employ the dual adaptive explicit time integration algorithm (DAETI) to ensure the solution's stability [34].

3. Numerical examples

Simulations for the numerical examples that are presented in the following were performed on a laptop with Intel® Core™ i7-4720HQ CPU and 16 GB of RAM. The efficiency of FPM was evaluated by comparing the execution time of FPM simulations with the execution time of FEM using linear elements. The execution time for both FPM and FEM for the considered numerical examples is summarized in Table 2. In all the examples, time integration is performed using the DAETI method [34], which employs the forward Euler method to solve explicitly both the diffusion and reaction operators with an adaptive time step. Solving the diffusion operator explicitly imposes a limit to the critical stable time step due to the conditional stability condition, which becomes smaller as the mesh resolution is increased. Applying a different adaptive scheme for the decoupled integration of the diffusion and reaction operators allows to perform the integration efficiently. For further details on the implementation of DAETI we refer the reader to the work in [34].

3.1. Electrical propagation in a 2D ventricular tissue

We considered a 4×4 cm human ventricular tissue with fibers aligned parallel to the x-axis. The longitudinal diffusion coefficient was

$d_0 = 0.0013$ cm^2/ms and the transverse-to-longitudinal conductivity ratio was $\rho = 0.15$. Electrophysiology was modeled by the O'Hara et al. [35] human ventricle action potential (AP) model for epicardial cells. Periodic stimuli of duration $t_d = 1$ ms and amplitude A equal to twice the diastolic threshold were applied on the left side of the tissue ($x = 0$ cm) at a frequency $f = 1$ Hz. AP propagation was simulated for a total time $t = 3$ s, after achievement of steady-state, using the DAETI method with time step $dt = 0.1$ ms.

Solutions obtained by FPM with different penalty coefficients, $p = \{1, 2, 5, 10\}$, were compared to a solution obtained by FEM with bilinear isoparametric elements (Fig. 2). For both FPM and FEM simulations, we considered four different nodal discretizations with spacing $\ell = \{0.25, 0.5, 1, 2\}$ mm, each of which is presented in one of the panels of Fig. 2. Differences between FEM and FPM solutions for each nodal discretization were evaluated in terms of conduction velocity (CV) and AP duration (APD) at 90% repolarization.

The maximum percentage difference between FPM and FEM in terms of CV was 116.9%, while in terms of APD_{90} it was 2.7% for nodal spacing $\ell = 2$ mm and $p = 10$. The minimum percentage difference between FPM and FEM in terms of CV was 7.1%, while in terms of APD_{90} it was 0.0% for nodal spacing $\ell = 0.25$ mm and $p = 1$. For a given nodal discretization, the best agreement between FEM and FPM solutions was always obtained for $p = 1$. For penalty factor values $p = 5$ and $p = 10$, the CV values obtained by FPM with coarse nodal discretizations $\ell = 2$ mm and $\ell = 1$ mm were in better agreement with the CV value obtained by FEM for a dense nodal discretization ($\ell = 0.25$ mm).

To evaluate the effect of the penalty coefficient, we performed a convergence analysis where we evaluated the relative error (ϵ_r) in CV for the solutions obtained by FPM with $p = \{1, 2, 5, 10\}$ with respect to the FEM solution for nodal spacing $\ell = \{0.25, 0.5, 1, 2\}$ mm:

$$\epsilon_r = \frac{CV_a - CV_e}{CV_e}, \tag{20}$$

where CV_a is the CV value obtained by FPM or FEM for each of the tested nodal discretizations and CV_e is the value obtained by FEM for a dense nodal discretization with $\ell = 0.1$ mm. The relative error, ϵ_r, for FPM with $p = 10$ and $p = 5$ was smaller than for FEM for coarse discretizations, but it was larger for finer discretizations (Fig. 3). For FPM with $p = 2$ and $p = 1$, ϵ_r decreased monotonically and its values
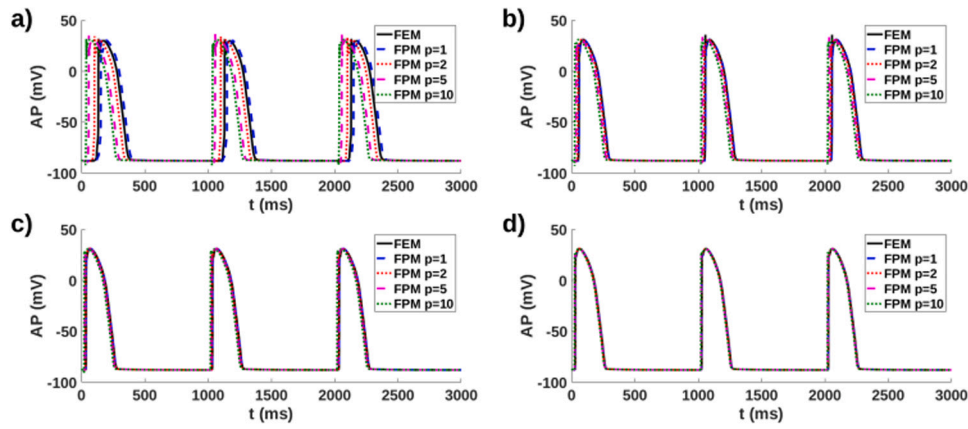
Fig. 2. AP propagation in 2D human ventricular tissue for FEM (black), FPM with penalty coefficient $p = 1$ (blue dashed), $p = 2$ (red dotted), $p = 5$ (magenta dashed) and $p = 10$ (green dotted). The four panels correspond to nodal discretizations with spacing ℓ of 0.25 mm (a), 0.5 mm (b), 1 mm (c) and 2 mm (d).
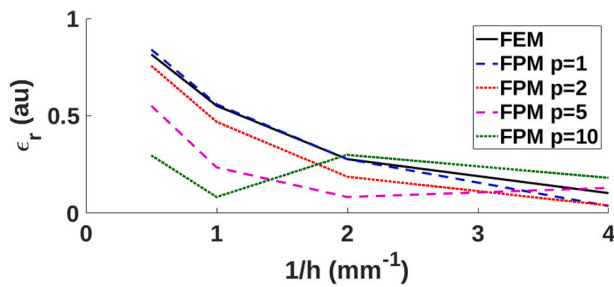

Fig. 3. Convergence analysis in terms of CV for FEM (black), FPM with penalty coefficient $p = 1$ (blue dashed), $p = 2$ (red dotted), $p = 5$ (magenta dashed) and $p = 10$ (green dotted).

Table 3
Activation times at the corners (P1–P8) and the center (C) of the 3D cuboid benchmark problem.

h (mm)	P1	P2	P3	P4	P5	P6	P7	P8	C
FPM activation time (ms)									
0.5	1	40	10	40	33	53	36	54	25
0.2	1	30	8	31	22	39	25	40	19
0.1	1	29	7	30	22	37	24	38	18
FEM activation time (ms) as in [34]									
0.5	1	49	22	58	94	109	98	111	54
0.2	1	31	11	35	35	51	39	54	25
0.1	1	29	8	31	27	41	29	43	20

were smaller than for FEM for practically all nodal spacing values. In the following numerical examples, we used $p = [1, 2]$.

3.2. Acetylcholine-induced effects in human atrial electrical activity

Acetylcholine-induced APD shortening in atrial myocytes facilitates the initiation and perpetuation of atrial fibrillation [36,37], which is a major risk factor for ischemic stroke. The parasympathetic neurotransmitter acetylcholine (ACh) shortens APD by activating the ACh-sensitive inward rectifier potassium current, I_{KACh}. Simulation of ACh-induced alterations in atrial electrophysiology is of interest in atrial fibrillation research [38].

Here, we considered a 2D atrial tissue of 4×4 cm with fibers aligned parallel to the X-axis in which ACh was distributed homogeneously throughout the tissue. The atrial myocyte electrophysiology was described using the Maleckar et al. model [39]. The longitudinal diffusion coefficient was set to $d_0 = 0.0035$ cm^2/ms and the transverse-to-longitudinal conductivity ratio was set to $\rho = 0.5$. The same periodic stimulation protocol as in Section 3.1 was simulated for $t_s = 3$ s and the DAETI method with time step $dt = 0.05$ ms was used to numerically solve AP propagation.

Simulations were performed using FPM with penalty coefficient $p = 1$ considering a regular nodal distribution with $\ell = 0.25$ mm and were compared with FEM simulations using bilinear isoparametric elements. The induced APD shortening was recorded at the center of the tissue for different ACh concentrations, $C_{ACh} = \{0.02, 0.04, 0.06, 0.08, 0.1\}$ μM (Fig. 4). APD shortening was found to range from 19 ms for the lowest ACh concentration to 38 ms for the highest ACh concentration. FPM results were found to be in good agreement with FEM, with differences of up to 2 ms. These results are in line with previous studies reporting APD shortening of up to 40 ms for $C_ACh = 0.1$ μM [36,40,41].

3.3. Electrical propagation in a benchmark 3D cuboid geometry

In this example, we solved the standard benchmark problem for verification of cardiac tissue electrophysiology simulators described in [42]. The problem's protocol considered the electrical stimulation of a 3D cuboid of human ventricular tissue with dimensions $3 \times 7 \times 20$ mm and cardiac fibers parallel to the Z axis. Epicardial cell electrophysiology was described by the Ten Tusscher et al. model [43] as in [42]. The longitudinal diffusion coefficient was set to $d_0 = 0.00115$ cm^2/ms and the transverse-to-longitudinal ratio was set to $\rho = 0.12$. A periodic stimulus with frequency $f = 1$ Hz, amplitude $A = 50$ mA and duration $t_d = 2$ ms was delivered at a cubic region with dimensions $1.5 \times 1.5 \times 1.5$ mm located at corner P1 (Fig. 5).

The activation time at the corners (P1–P8) and the center (C) of the cuboid were recorded for three different nodal discretizations, $\ell = \{0.1, 0.2, 0.5\}$ mm, for a simulation using FPM with penalty coefficient $p = 1$. Integration was performed using the DAETI method with time step $dt = 0.1$ ms. The activation times obtained by FPM were compared with those of FEM (Table 3) previously reported in [34] and validated with the reported activation times in [42].

The activation times for FPM and FEM for nodal spacing $\ell = 0.1$ mm were found to be in good agreement. For coarse nodal discretizations, the FEM solution led to larger activation times as compared to FPM, especially at points **P5–P8**. Activation times at **P7** for FEM simulations were found to be ×2.37 larger for the spacing $\ell = 0.5$ mm than for the spacing $\ell = 0.1$ mm. On the other hand, this difference was found to be ×1.5 for FPM simulations. For a nodal spacing $\ell = 0.2$ mm, activation times were notably closer to those of $\ell = 0.1$ mm when using FPM than when using FEM. These results illustrate the improved accuracy of FPM for coarse nodal discretizations and are in good agreement with the findings in Section 3.1.
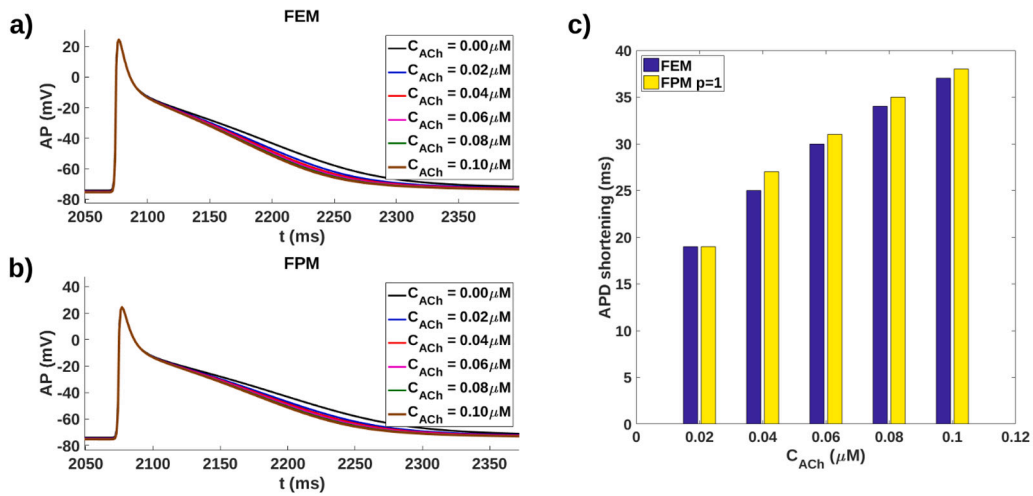
Fig. 4. APs at the center of a 4×4 cm atrial tissue for different ACh concentrations obtained from (a) FEM and (b) FPM simulations. (c) APD shortening induced by acetylcholine concentration for FEM (blue) and FPM (yellow) simulations.
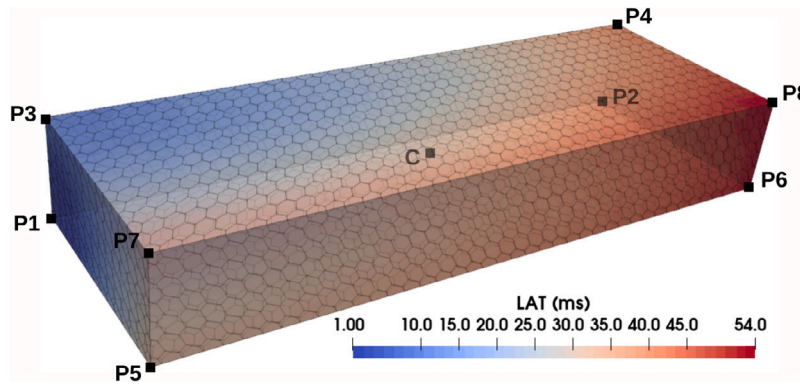

Fig. 5. Local activation time (LAT) map for the 3D cuboid benchmark geometry described in [42] with space discretization $\ell = 0.5$ mm.

3.4. Simulation of electrical activation in a 3D biventricular infarction model

We employed the FPM method to simulate AP propagation in a 3D biventricular model under myocardial infarction conditions and we compared the activation pattern obtained by FPM with the one obtained by FEM. We considered a simplified model where zero conduction was assumed for the scar tissue, while border zone effects were not taken into account.

The biventricular anatomy was constructed using ex vivo diffusion weighted imaging (DWI) of a porcine heart. The two ventricles of the heart were manually segmented and a scar was introduced at the septal-anterior wall of the left ventricle (Fig. 6). A tetrahedral mesh (nodes: 70521, elements: 311150) was generated from the segmented data using iso2mesh [44]. FPM cells were generated for the nodes of the tetrahedral mesh using a dual polyhedral mesh generation algorithm [45, 46]. Fiber direction was determined by computing the diffusion tensors using an algorithm based on Riemannian distances [47].

Cell electrophysiology was modeled by the O'Hara et al. model [35] considering endocardium:midmyocardium:epicardium with 50:20:30 ratio. Pacing was performed by applying a periodic stimulus with amplitude equal to twice the diastolic threshold and frequency $f = 1$ Hz at two tested stimulation regions: one at the base of the model located at the anterior wall of the right ventricular base near the septum and the other one at the apex of the left ventricle (Fig. 6).

The local activation time (LAT) at each node of the model was computed using FPM with penalty coefficient $p = 1.5$ and it was compared with the LAT value obtained from a FEM simulation. Mean LAT for basal pacing was 170 ms for FPM and 173 ms for FEM, while
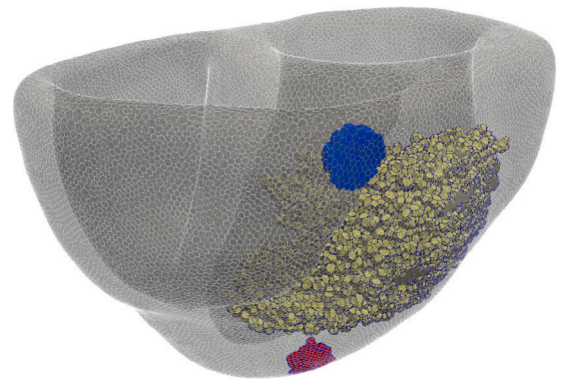

Fig. 6. Biventricular model depicting the infarcted region (yellow), the basal pacing region (blue) and the apical pacing region (red).

mean LAT for apical pacing was 151 ms for FPM and 148 ms for FEM. The LAT histograms presented in Fig. 7 demonstrate the good agreement between FPM and FEM simulations, with FPM rendering a valuable alternative to FEM for large scale cardiac electrophysiology simulations.

4. Concluding remarks

In this work, we presented the Fragile Points Method (FPM) for in silico cardiac electrophysiology applications. Despite being common for
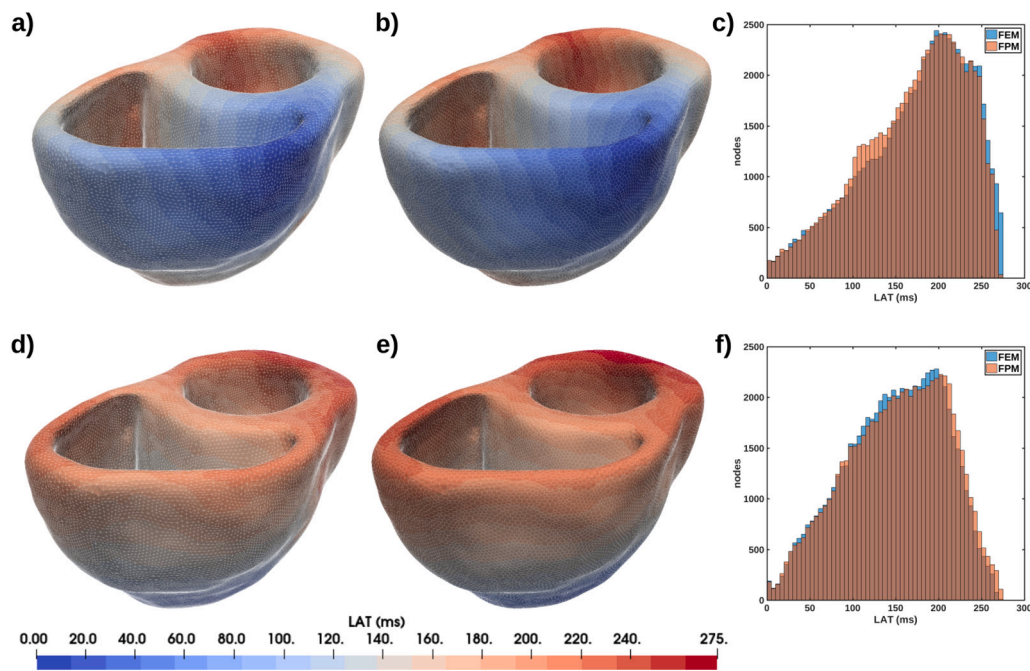
Fig. 7. LAT for (a) basal pacing using FEM, (b) basal pacing using FPM with $p = 1.5$, (d) apical pacing using FEM, (e) apical pacing using FPM with $p = 1.5$. Comparisons of LAT histograms are shown for basal pacing in (c) and for apical pacing in (f).

meshless methods to sacrifice efficiency for accuracy or vice versa, FPM was proven to achieve similar accuracy and efficiency to FEM (Table 2).

We found that solutions obtained by FPM were in good agreement with FEM for both 2D and 3D scenarios, allowing to simulate action potential propagation with high accuracy under different physiological and pathological conditions. FPM demonstrated comparable convergence to FEM (Table 3), in line with previous findings. This may have an important role in large scale applications where FPM could increase time efficiency without losing accuracy by alleviating the requirement for a good quality mesh. By adjusting the penalty coefficient, improved solutions could be obtained even for coarse discretizations. However, for large values of the penalty coefficient (p) accuracy could be deteriorated for fine discretizations. We found $p = [1, 2]$ to lead to accurate results for all discretizations.

It should be noted that here we compared FPM with FEM for the decoupled monodomain model after using the operator splitting technique. We used an in-house solver based on the DAETI method [34] for explicit time integration, in which we used either FPM or FEM to construct the diffusion operator. While the decoupled monodomain model has been widely used in cardiac electrophysiology due to its high efficiency and ease of implementation, it has been reported to lead to less accurate results than the fully coupled model [48]. Sophisticated solvers that employ execution parallelism and provide optimal memory usage [49] have been proposed to enable solving the coupled problem efficiently [50]. Such solutions allow simulating electrophysiology with higher accuracy while maintaining efficiency by solving FEM-based algebraic systems using preconditioning techniques. We expect FPM to be a promising alternative to FEM for coupled solvers too. We base this claim on the fact that FPM leads to sparse and symmetric matrices as in FEM. Therefore, solvers and preconditioners that have been developed for FEM could be used directly to solve FPM-based algebraic systems.

Finally, the ability of FPM to provide similar accuracy and efficiency to FEM without requiring mesh connectivity information renders the method an interesting alternative to FEM, particularly for personalized image-based modeling applications.

CRediT authorship contribution statement

Konstantinos A. Mountris: Conception and design of study, Acquisition of data, Analysis and/or interpretation of data, Writing – original draft, Writing – review & editing. **Esther Pueyo:** Conception and design of study, Acquisition of data, Analysis and/or interpretation of data, Writing – review & editing.

Declaration of competing interest

The authors declare that they have no known competing financial interests or personal relationships that could have appeared to influence the work reported in this paper.

Acknowledgments

References

[1] E.A. Heidenreich, J.M. Ferrero, M. Doblaré, J.F. Rodríguez, Adaptive macro finite elements for the numerical solution of monodomain equations in cardiac electrophysiology, Ann. Biomed. Eng. 38 (7) (2010) 2331–2345.

[2] D. Eppstein, Global optimization of mesh quality, in: Tutorial at the 10th International Meshing Roundtable, vol. 10, (no. 2001) 2001, p. 13.

[3] T. Belytschko, Y.Y. Lu, L. Gu, Element-free Galerkin methods, Internat. J. Numer. Methods Engrg. 37 (2) (1994) 229–256.

[4] T. Belytschko, Y. Krongauz, D. Organ, M. Fleming, P. Krysl, Meshless methods: An overview and recent developments, Comput. Methods Appl. Mech. Engrg. 139 (1–4) (1996) 3–47.

[5] G.-R. Liu, D. Karamanlidis, Mesh free methods: Moving beyond the finite element method, Appl. Mech. Rev. 56 (2) (2003) B17–B18.

[6]   H. Zhang, H. Ye, W. Huang, A meshfree method for simulating myocardial electrical activity, Comput. Math. Methods Med. 2012 (2012).

[7]   P. Lancaster, K. Salkauskas, Surfaces generated by moving least squares methods, Math. Comp. 37 (155) (1981) 141–158.

[8]   M. Arroyo, M. Ortiz, Local maximum-entropy approximation schemes, in: Meshfree Methods for Partial Differential Equations III, Springer, 2007, pp. 1–16.

[9]   D. Millán, N. Sukumar, M. Arroyo, Cell-based maximum-entropy approximants, Comput. Methods Appl. Mech. Engrg. 284 (2015) 712–731.

[10] K.A. Mountris, G.C. Bourantas, D. Millán, G.R. Joldes, K. Miller, E. Pueyo, A. Wittek, Cell-based maximum entropy approximants for three-dimensional domains: Application in large strain elastodynamics using the meshless total Lagrangian explicit dynamics method, Internat. J. Numer. Methods Engrg. 121 (3) (2020) 477–491.

[11] J. Dolbow, T. Belytschko, Numerical integration of the Galerkin weak form in meshfree methods, Comput. Mech. 23 (3) (1999) 219–230.

[12] I. Babuška, U. Banerjee, J.E. Osborn, Q. Li, Quadrature for meshless methods, Internat. J. Numer. Methods Engrg. 76 (9) (2008) 1434–1470.

[13] K.A. Mountris, E. Pueyo, The radial point interpolation mixed collocation method for the solution of transient diffusion problems, Eng. Anal. Bound. Elem. 121 (2020) 207–216.

[14] K.A. Mountris, E. Pueyo, Cardiac electrophysiology meshfree modeling through the mixed collocation method, 2021, arXiv preprint arXiv:2110.06671.

[15] K.A. Mountris, C. Sanchez, E. Pueyo, A novel paradigm for in silico simulation of cardiac electrophysiology through the mixed collocation meshless Petrov-Galerkin method, in: 2019 Computing in Cardiology, CinC, IEEE, 2019, pp. Page–1.

[16] K.A. Mountris, E. Pueyo, Next-generation in silico cardiac electrophysiology through immersed grid meshfree modeling: Application to simulation of myocardial infarction, in: 2020 Computing in Cardiology, IEEE, 2020, pp. 1–4.

[17] S.N. Atluri, H.T. Liu, Z.D. Han, Meshless local Petrov-Galerkin (MLPG) mixed collocation method for elasticity problems, CMC-Tech Science Press- 4 (3) (2006) 141.

[18] T. Zhang, Y. He, L. Dong, S. Li, A. Alotaibi, S.N. Atluri, Meshless local Petrov-Galerkin mixed collocation method for solving cauchy inverse problems of steady-state heat transfer, CMES Comput. Model. Eng. Sci. 97 (6) (2014) 509–553.

[19] S. Li, S. Atluri, The MLPG mixed collocation method for material orientation and topology optimization of anisotropic solids and structures, CMES Comput. Model. Eng. Sci. 30 (1) (2008) 37–56.

[20] N. Libre, A. Emdadi, E. Kansa, M. Rahimian, M. Shekarchi, A stabilized RBF collocation scheme for Neumann type boundary value problems, CMES - Comput. Model. Eng. Sci. 24 (1) (2008) 61–80.

[21] L. Dong, T. Yang, K. Wang, S.N. Atluri, A new fragile points method (FPM) in computational mechanics, based on the concepts of point stiffnesses and numerical flux corrections, Eng. Anal. Bound. Elem. 107 (2019) 124–133.

[22] T. Liszka, J. Orkisz, The finite difference method at arbitrary irregular grids and its application in applied mechanics, Comput. Struct. 11 (1–2) (1980) 83–95.

[23] D.N. Arnold, F. Brezzi, B. Cockburn, L.D. Marini, Unified analysis of discontinuous Galerkin methods for elliptic problems, SIAM J. Numer. Anal. 39 (5) (2002) 1749–1779.

[24] T. Yang, L. Dong, S.N. Atluri, A simple Galerkin meshless method, the fragile points method using point stiffness matrices, for 2D linear elastic problems in complex domains with crack and rupture propagation, Internat. J. Numer. Methods Engrg. 122 (2) (2021) 348–385.

[25] Y. Guan, R. Grujicic, X. Wang, L. Dong, S.N. Atluri, A new meshless "fragile points method" and a local variational iteration method for general transient heat conduction in anisotropic nonhomogeneous media. Part II: Validation and discussion, Numer. Heat Transfer B 78 (2) (2020) 86–109.

[26] Y. Guan, S.N. Atluri, Meshless fragile points methods based on Petrov-Galerkin weak-forms for transient heat conduction problems in complex anisotropic nonhomogeneous media, 2021, arXiv preprint arXiv:2101.08897.

[27] Y. Guan, L. Dong, S.N. Atluri, A new meshless fragile points method (FPM) with minimum unknowns at each point, for flexoelectric analysis under two theories with crack propagation. Part I: Theory and implementation, 2020, arXiv preprint arXiv:2011.06412.

[28] E. Oñate, F. Perazzo, J. Miquel, A finite point method for elasticity problems, Comput. Struct. 79 (22–25) (2001) 2151–2163.

[29] S. Tiwari, J. Kuhnert, Finite pointset method based on the projection method for simulations of the incompressible Navier-Stokes equations, in: Meshfree Methods for Partial Differential Equations, Springer, 2003, pp. 373–387.

[30] M. Liu, W. Xie, G. Liu, Modeling incompressible flows using a finite particle method, Appl. Math. Model. 29 (12) (2005) 1252–1270.

[31] J.P. Keener, J. Sneyd, Mathematical Physiology: Systems Physiology. II, Springer, 2009.

[32] H.J. Schroll, G.T. Lines, A. Tveito, On the accuracy of operator splitting for the monodomain model of electrophysiology, Int. J. Comput. Math. 84 (6) (2007) 871–885.

[33] I. Mozolevski, E. Süli, P.R. Bösing, Hp-version a priori error analysis of interior penalty discontinuous Galerkin finite element approximations to the biharmonic equation, J. Sci. Comput. 30 (3) (2007) 465–491.

[34] K.A. Mountris, E. Pueyo, A dual adaptive explicit time integration algorithm for efficiently solving the cardiac monodomain equation, Int. J. Numer. Methods Biomed. Eng. (2021) e3461.

[35] T. O'Hara, L. Virág, A. Varró, Y. Rudy, Simulation of the undiseased human cardiac ventricular action potential: Model formulation and experimental validation, PLoS Comput. Biol. 7 (5) (2011).

[36] J.D. Bayer, B.J. Boukens, S.P. Krul, C.H. Roney, A.H. Driessen, W.R. Berger, N.W. van den Berg, A.O. Verkerk, E.J. Vigmond, R. Coronel, et al., Acetylcholine delays atrial activation to facilitate atrial fibrillation, Front. Physiol. 10 (2019) 1105.

[37] J. Smeets, M.A. Allessie, W. Lammers, F. Bonke, J. Hollen, The wavelength of the cardiac impulse and reentrant arrhythmias in isolated rabbit atrium. The role of heart rate, autonomic transmitters, temperature, and potassium, Circ. Res. 58 (1) (1986) 96–108.

[38] C. Celotto, C. Sánchez, K.A. Mountris, P. Laguna, E. Pueyo, Location of Parasympathetic Innervation Regions from electrograms to guide atrial fibrillation ablation therapy: An in silico modeling study, Front. Physiol. 12 (2021) 1020.

[39] M.M. Maleckar, J.L. Greenstein, N.A. Trayanova, W.R. Giles, Mathematical simulations of ligand-gated and cell-type specific effects on the action potential of human atrium, Prog. Biophys. Mol. Biol. 98 (2–3) (2008) 161–170.

[40] C. Celotto, C. Sánchez, P. Laguna, E. Pueyo, Calcium-activated potassium channels inhibition in autonomically stimulated human atrial myocytes, in: 2019 Computing in Cardiology, CinC, IEEE, 2019, pp. Page–1.

[41] C. Celotto, C. Sánchez, K.A. Mountris, P. Laguna, E. Pueyo, SK channel block and adrenergic stimulation counteract acetylcholine-induced arrhythmogenic effects in human atria, in: 2020 42nd Annual International Conference of the IEEE Engineering in Medicine & Biology Society, EMBC, IEEE, 2020, pp. 2303–2306.

[42] S.A. Niederer, E. Kerfoot, A.P. Benson, M.O. Bernabeu, O. Bernus, C. Bradley, E.M. Cherry, R. Clayton, F.H. Fenton, A. Garny, et al., Verification of cardiac tissue electrophysiology simulators using an N-version benchmark, Phil. Trans. R. Soc. A 369 (1954) (2011) 4331–4351.

[43] K.H. Ten Tusscher, A.V. Panfilov, Alternans and spiral breakup in a human ventricular tissue model, Am. J. Physiol.-Heart Circ. Physiol. 291 (3) (2006) H1088–H1100.

[44] Q. Fang, D.A. Boas, Tetrahedral mesh generation from volumetric binary and grayscale images, in: 2009 IEEE International Symposium on Biomedical Imaging: From Nano To Macro, Ieee, 2009, pp. 1142–1145.

[45] R.V. Garimella, J. Kim, M. Berndt, Polyhedral mesh generation and optimization for non-manifold domains, in: Proceedings of the 22nd International Meshing Roundtable, Springer, 2014, pp. 313–330.

[46] J. Kim, An efficient approach for solving mesh optimization problems using Newton's method, Math. Probl. Eng. 2014 (2014).

[47] A. Barmpoutis, B.C. Vemuri, A unified framework for estimating diffusion tensors of any order with symmetric positive-definite constraints, in: 2010 IEEE International Symposium on Biomedical Imaging: From Nano to Macro, IEEE, 2010, pp. 1385–1388.

[48] P.C. Franzone, L. Pavarino, S. Scacchi, A comparison of coupled and uncoupled solvers for the cardiac bidomain model, ESAIM Math. Model. Numer. Anal. 47 (4) (2013) 1017–1035.

[49] N. Chamakuri, P. Kügler, A coupled monodomain solver with optimal memory usage for the simulation of cardiac wave propagation, Appl. Math. Comput. 378 (2020) 125212.

[50] M. Murillo, X.-C. Cai, A fully implicit parallel algorithm for simulating the nonlinear electrical activity of the heart, Numer. Linear Algebra Appl. 11 (2–3) (2004) 261–277.
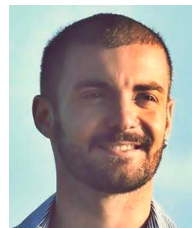
Konstantinos A. Mountris received a Ph.D. degree (in 2017) in Technology for Health Science & Biology from University of Western Brittany (Brest, FR). Currently, he is a Marie Curie Postdoc Research Fellow at the University College London, London, United Kingdom. His current focus is the development of computational models based on Finite Elements Method and Meshless Methods for problems arising in cardiac electrophysiology.